Atmos. Chem. Phys. Discuss., https://doi.org/10.5194/acp-2019-322
Manuscript under review for journal Atmos. Chem. Phys.
Discussion started: 7 May 2019

Atmospheric Chemistry and Physics Discussions

Detection of land surface induced atmospheric water vapor patterns

Tobias Marke[1], Ulrich Löhnert[1], Vera Schemann[1], and Susanne Crewell[1]
[1]Institute for Geophysics and Meteorology, University of Cologne, Germany
Correspondence: Tobias Marke tmarke@meteo.uni-koeln.de

Abstract. Finding observational evidence of land surface atmosphere interactions is crucial for understanding the spatial and temporal evolution of the boundary layer, as well as for model evaluation, in particular large-eddy simulation (LES) models. In this study, the influence of a heterogeneous land surface on the spatial distribution of atmospheric water vapor is assessed. Ground-based remote sensing measurements of a scanning microwave radiometer (MWR) are used in a long-term study over six years to characterize spatial heterogeneities in integrated water vapor (IWV) during clear sky conditions at the Jülich Observatory for Cloud Evolution (JOYCE). The resulting deviations from the mean of the scans reveal a direction-dependent IWV that is visible throughout the day. Comparisons to a satellite derived spatial IWV distribution show a good agreement for a selection of 61 satellite overpasses during convective situations. With the help of a land use type classification and information on the topography, the main type for the regions with a positive IWV deviation was determined to be agricultural fields and nearby open pit mines. Negative deviations occurred mainly above elevated forests and urban areas. The observational results are in agreement with a high resolution large-eddy simulation (LES), which was used in addition to investigate changes in surface fluxes and the water vapor and cloud field for an altered land use input.

1 Introduction

Interactions between compartments of land surface and the atmospheric boundary-layer can have significant influences on the regional weather and climate. Heterogeneity in land use, among other parameters characterized by soil type, vegetation and urban areas, induces spatial variability in surface fluxes of momentum, sensible and latent heat. Numerical studies suggest, that contrasts in land surface fluxes are responsible for mesoscale circulations and considerably affect the state of the atmospheric boundary-layer in a non-linear way (e.g. Ookouchi et al., 1984; Pielke et al., 1991; Clark and Arritt, 1995). Furthermore the transport of energy and water vapor into the atmosphere can trigger the formation of shallow convective clouds and precipitation (e.g. Rabin et al., 1990; Avissar and Schmidt, 1998). Because this small scale variability can not be resolved by most weather forecast and climate models, it needs to be parameterized. This requires assumptions near compartment boundaries, which strongly affects exchange processes. Unresolved patterns in the models are crucial, since the resulting gradients directly influence the fluxes and hence the evolution of the model state (Simmer et al., 2015). Monitoring and modeling these spatial

patterns and compartment interactions is the main focus of this study, which is related to the Transregional Collaborative Research Centre 32 (TR32) "Patterns in Soil-Vegetation-Atmosphere Systems" (www.tr32.de).

Since the scales of surface heterogeneity and resulting interaction processes with the overlying boundary-layer are in the order meters to kilometers, a frequently used tool for studying these interaction processes on a local scale is conducting high resolution large-eddy simulations (LES) (e.g. Courault et al., 2007; Huang and Margulis, 2009; Maronga and Raasch, 2013; Shao et al., 2013). By altering the land surface properties, the turbulence resolving simulations provide estimates of the resulting effect on the boundary-layer structure. In this way Vilà-Guerau De Arellano et al. (2014) found differences in cloud dynamics that can be related to the partitioning of the surface fluxes determined by the plant functional type. In van Heerwaarden and Guerau de Arellano (2008) an enhancement of cloud formation over heterogeneous landscapes using different Bowen ratios is indicated.

For a better understanding of the influence of the land surface on the atmospheric state and in order to evaluate model findings, ground-based observations by current state-of-the-art remote sensing instrumentation can be used. Significant effects of heterogeneous land use on the turbulent fluxes and connections to clouds have been shown in several field campaigns in a short-term perspective (Weckwerth et al., 2004; Beyrich et al., 2006; Wulfmeyer et al., 2011; Späth et al., 2016; Macke et al., 2017; Wulfmeyer et al., 2018). Investigating the influence of land use heterogeneity on boundary-layer characteristics, such as water vapor and clouds, from long-term measurements can play a key role in finding systematically significant patterns in relations between the local land surface and atmosphere above.

As a key parameter that connects vegetation activity and the boundary-layer, the atmospheric water vapor plays an important role within the hydrological cycle, but also for the energy balance at the surface and within the atmosphere. Späth et al. (2016) investigated water vapor fields for a limited amount of time in a campaign with a scanning differential absorption lidar and found gradients related to surface elevation and land cover type. But also long-term studies of the spatiotemporal variability of water vapor already revealed terrain-related processes in a mountainous area (Adler et al., 2016) by using scans of a passive ground-based microwave radiometer (MWR). Compared to the widely used satellite observations for spatially resolved water vapor estimates, available only for a handful of overpasses per day, the MWR is well suited for continuous and temporally highly resolved measurements at a certain location. While MWR profile measurements of humidity suffer from a coarse resolution, a good agreement between zenith measurements of integrated water vapor (IWV) using MWR, satellite and Global Positioning System (GPS) observations was shown in Steinke et al. (2015). Also, the MWR has already proven to be able to detect horizontal humidity gradients by retrieving IWV values in a scanning configuration (Kneifel et al., 2009; Schween et al., 2011).

To address the question whether spatial water vapor distributions can be connected to land surface properties, this observational and modeling study focuses on the long-term pattern of azimuthal IWV deviations derived from satellite and

Atmos. Chem. Phys. Discuss., https://doi.org/10.5194/acp-2019-322
Manuscript under review for journal Atmos. Chem. Phys.
Discussion started: 7 May 2019

ground-based measurements at the Jülich ObservatorY of Cloud Evolution (JOYCE, Löhnert et al. (2015)) in Western Germany (50.91°N, 6.41°E). At JOYCE, various remote sensing instruments, including a scanning MWR, are deployed since 2011 to continuously monitor water vapor, clouds and precipitation. For comparing the spatial IWV distribution derived from the MWR with an independent measurement, a satellite water vapor product is used at high spatial resolution. In addition, a Doppler wind lidar is available for a characterization of the atmospheric boundary-layer in terms of the winds and turbulent mixing processes that control the exchange of water vapor between the surface and the atmosphere. The impact of the land surface on the atmospheric water vapor distribution is evaluated by the comparison of the derived IWV deviations to a detailed land use map. To better understand which process explains the observed water vapor anomalies, sensitivity studies with high resolution LES are performed with different land use type settings.

The description of the utilized instruments and data of this study in Sect. 2 is followed by the analysis of the IWV deviations obtained from long-term MWR scans, selected during clear-sky conditions (Sect. 3.1). For a better description of the state of the boundary-layer and large scale effects, the results are presented together with wind and turbulence statistics derived from Doppler lidar measurements during the MWR scans and a reanalysis product. Subsequently, the IWV deviations derived from MWR scans and satellite observations are compared for a collection of overpasses (Sect. 3.2). A case study comparing the satellite and ground-based results is complemented by the analysis of two large-eddy simulations focusing on the land use influence on the atmospheric water vapor (Sect. 3.3) and a summary of the results is given in Sect. 4.

2 Instruments and data

2.1 Microwave radiometer

The microwave radiometer HATPRO (Humidity And Temperature PROfiler) at JOYCE utilizes direct detection receivers and measures the brightness temperatures (TB) at 7 channels in the K-band from 22 GHz to 32 GHz and at 7 channels also in the V-band from 52 GHz to 58 GHz. In this study, the observations of the 7 K-band channels with a 1–2 s temporal resolution are taken into account. A statistical approach based on a least squares linear regression model (Löhnert and Crewell, 2003) is applied to derive IWV, absolute humidity (q) and liquid water path (LWP) using observations of the downwelling microwave radiance along the water vapor absorption line between 22.24 and 27.84 GHz and in the atmospheric window at 31.4 GHz. The instrument is capable of observing in high temporal resolutions (Rose et al., 2005) and the absolute error in zenith TB measurements of 0.5 K is mainly determined by the instrument absolute calibration (Maschwitz et al., 2013). This accuracy converts into an uncertainty of 0.5–0.8 $\mathrm{kg\ m^{-2}}$ in the derived IWV and 20–30 $\mathrm{g\ m^{-2}}$ for LWP.

The zenith measurements ($\mathrm{IWV_z}$) alternate with full azimuth scans in 10° steps at 30° elevation angle. The scans are available between June 2012–June 2015 and starting from June 2018. In 2016 and 2017 no MWR scans were performed. The scanning frequency is 15 min and is increased to 10 min between 25 June and 18 July 2018 and decreased to 30 min after 18 July 2018. Due to directional dependent interference in the unprotected 26.24 GHz channel, specific azimuth directions are not

Atmos. Chem. Phys. Discuss., https://doi.org/10.5194/acp-2019-322
Manuscript under review for journal Atmos. Chem. Phys.
Discussion started: 7 May 2019

considered (50°, 160°, 180°, 260°) and missing values are filled using a linear interpolation. For all scans, the derived values for LWP, IWV and q are air-mass corrected to account for the slant angle of the scanning MWR.

2.2 Doppler lidar and boundary-layer classification

As a pulsed lidar system, the Halo Photonics Streamline Doppler lidar (Pearson et al., 2009) provides range-resolved profile measurements of radial Doppler velocity and backscattered signal. With a wavelength of 1.5 μm (near-IR) the instrument is sensitive to the backscatter of aerosols and clouds and is able to scan the full hemisphere. The maximum detectable range depends on the presence of atmospheric particles and the lowest reliable range is at 105 m. At JOYCE the system is set to a range resolution of 30 m and performs plan position indicator scans every 15 min to estimate wind speed and direction profiles based on the velocity-azimuth display (VAD) method using 36 beams at 75° elevation. In addition the Doppler beam swing (DBS) technique with three beams and range height indicator scans are scheduled every 5 min and 30 min, respectively. The remaining time, the instrument is staring zenith to derive the vertical velocity with high temporal resolution (1 s).

To study land surface atmosphere exchange processes it is crucial to know the turbulent state of the boundary-layer. Therefore an objective classification of the mixing sources presented by Manninen et al. (2018) is utilized to describe the turbulence characteristics during MWR scans at JOYCE. The method is based on the combination of multiple Doppler lidar quantities including the dissipation rate of turbulent kinetic energy (TKE) derived from vertically pointing observations using the method presented in O'Connor et al. (2010). The TKE dissipation rate is based on the variance of the observed mean Doppler velocity and allows for a threshold based estimation of the convective boundary-layer (CBL) height.

2.3 MODIS IWV

The passive, imaging Moderate Resolution Imaging Spectroradiometer (MODIS) measures in 36 spectral bands ranging from 0.4 μm to 14.4 μm. Two MODIS instruments are currently airborne on NASA's sun-synchronous near-polar-orbiting Earth Observing System Terra and Aqua satellites. A full coverage of the globe is achieved in 1–2 days with an orbit height of 705 km and a scan rate of 20.3 rpm. The swath dimension of MODIS is 2330 km (cross track) and 10 km (along track at nadir). Within the 36 spectral bands, five channels in the 0.8–1.3 μm near-infrared spectral region can be used for water vapor remote sensing (Gao and Kaufman, 2003). For IWV estimates the Level-2 (Collection 6.1) near-infrared retrieval (MODIS-NIR) with a 1 km spatial resolution is chosen. The retrieval by Gao and Kaufman (2003) is based on three channels at 0.936 μm, 0.940 μm and 0.905 μm for the water vapor absorption and at 0.865 μm and 1.24 μm to correct for atmospheric gaseous absorption. In order to derive the total vertical amount of water vapor, the reflected NIR solar radiation in the water vapor absorption channel is compared to the window channels yielding the atmospheric water vapor transmittance. The amount of water vapor is then obtained from look-up tables derived from a line-by-line atmospheric transmittance code. Reliable estimates of the water vapor total column amount over land areas can only be inferred during daytime and for cloud free regions. Typical errors of the MODIS-NIR water vapor product range between 5–10%. Here, a height correction similar to Steinke et al. (2015) of the

retrieved values is performed due to the variations of the horizontal and height distance to JOYCE per flight track of MODIS. The height difference is corrected by assuming an exponential decrease of the humidity profile and by using the water vapor density obtained from measurements of temperature, humidity and pressure of a weather sensor attached to the MWR and the topography with a 200 m horizontal resolution. Furthermore, the IWV product was resampled to 100 m for calculating the mean values of several overpasses.

2.4 ERA5 data products

To distinguish between local influences and large scale features regarding the observed spatial pattern of IWV deviations, the reanalysis products of ERA5 with a 31 km horizontal resolution are analyzed (Copernicus Climate Change Service (C3S), 2017). Besides the u and v wind components at different pressure levels (1000 hPa, 700 hPa), also the direction of the IWV transport (IWVT, in degree) is considered at a 3 h temporal resolution for the closest point to JOYCE. The vertical integral of water vapor flux, used to derive IWVT, is calculated utilizing the specific humidity and winds on model levels. The ERA5 IWV is selected at the closest output time to the MWR scans.

2.5 ICON-LEM

As a state-of-the-art atmospheric modeling system, the ICOsahedral Non-hydrostatic model ICON (Zängl et al., 2015) has been developed by the German Weather Service (DWD) and the Max Planck Institute for Meteorology (MPI-M). The ICON Large-Eddy Model (ICON-LEM) was designed within the framework of the High Definition Clouds and Precipitation for advancing Climate Prediction (HD(CP)^2) project for improving moist processes in climate prediction models (Heinze et al., 2017). In this study, the ICON-LEM simulations are used to provide a spatial representation of the IWV field to compare with the measurements obtained from the scanning MWR and the MODIS-NIR water vapor product around JOYCE.

A good agreement between simulations of ICON-LEM using high grid resolutions of up to 156 m and observations was already shown in Heinze et al. (2017) concerning turbulence, column water vapor and cumulus clouds (compared to satellite observations). Also the topographic influence on the wind field was shown in ICON-LEM simulations and observations at JOYCE (Marke et al., 2018). Therefore a similar setup with a domain radius size of 10 km, 78 m horizontal resolution and 20 km vertical extent is used in this study. The minimal layer thickness is 20 m and the lowest 2 km contain 33 levels. As forcing data, the ECMWF Integrated Forecasting System (IFS) model is used. In addition to the control simulation using a simplified version of the land use input data GLOBCOVER (Bontemps et al., 2011) with a 300 m resolution, a second simulation is conducted with an altered land use setting. In this way parameters like leaf area index and roughness length are changed to get a different distribution of potential water vapor sources and sinks at the surface.

Atmos. Chem. Phys. Discuss., https://doi.org/10.5194/acp-2019-322
Manuscript under review for journal Atmos. Chem. Phys.
Discussion started: 7 May 2019

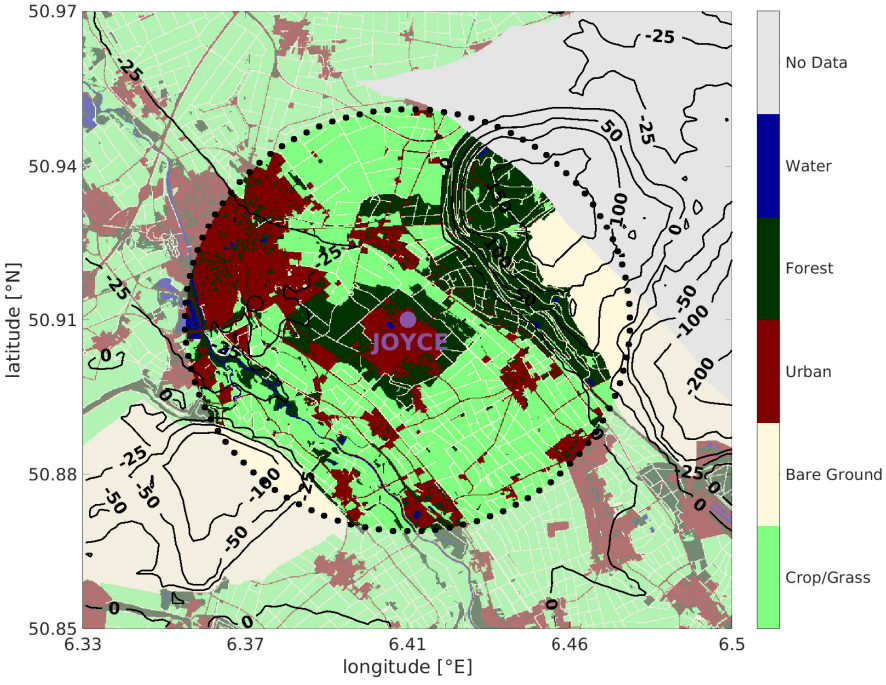

Figure 1. Simplified map (12x13 km) of the land use classification described in Waldhoff et al. (2017) centered around JOYCE. The highlighted area (4.3 km radius) shows the crossing distance of the MWR scans at the IWV scaling height of 2.5 km. Contours refer to the height relative to JOYCE (111 m a.s.l.).

2.6 Land use classification and measurement site description

To be able to link atmospheric water vapor measurements with land surface properties, spatial land use information is needed. This is addressed by using a remote sensing-based regional crop map (Waldhoff et al., 2017) that was applied to a study area in Western Germany including the surrounding area of JOYCE. In this method, supervised multi-temporal remote sensing data of Sentinel-2, ancillary information and expert-knowledge on crops are combined in a Multi-Data Approach (MDA). The classification is therefore able to differentiate between 44 vegetated, urban and water areas with a spatial resolution of 15 m.

The detailed and highly resolved classification is used to identify areas with a predominant land use type. Therefore the classified types are condensed into five main types, in particular agricultural areas and grass land, bare ground, urban areas, deciduous forest and water. These five groups are expected to have a significantly different behavior in terms of transpiration and/or evaporation and therefore might cause atmospheric water vapor patterns that can be distinguished and related to the appropriate type. In Fig. 1 the simplified land use classification of a 12x13 km area centered around JOYCE is shown. The

Atmos. Chem. Phys. Discuss., https://doi.org/10.5194/acp-2019-322
Manuscript under review for journal Atmos. Chem. Phys.
Discussion started: 7 May 2019

Atmospheric Chemistry and Physics Discussions

city of Jülich to the northwest but also JOYCE at the Research Center Jülich are the largest urban areas in this surrounding. The artificially created pit mine dump hill Sophienhöhe is located in the northeast direction, which is up to 200 m higher than JOYCE and covered mainly by a deciduous forest. In the northern and southeastern part of the selected domain mostly agricultural sites can be identified. The main crop types between April and September are winter wheat and sugar beet, but also maize and potato. A common crop rotation is a two year cycle of sugar beet to winter wheat (Waldhoff et al., 2017). The southwestern parts are mostly grass lands surrounding the Rur River, with its valley going from southeast to northwest. The pit mines (bare ground) with depressions down to 300 m below JOYCE are located to the east and southwest.

3 Results

3.1 Long-term MWR scans and boundary-layer characteristics

In order to find patterns in the long-term water vapor scans at JOYCE, that can be related to local land surface characteristics, the MWR scans are evaluated during meteorological conditions that are favorable for strong land surface atmosphere interactions. This excludes overcast situations and large scale advection of moist or dry air. The cloud detection is obtained by using the 31.4 GHz channel, which is within an atmospheric window. The signal from this channel is dominated by the presence of liquid water in case of clouds appearing in the instrument's field of view. During a single scan the maximum difference of the measured 31.4 GHz brightness temperature for each azimuth direction and the mean of the whole scan must be below 2 K, since liquid water clouds are expected to cause a much higher difference. Furthermore the air-mass corrected LWP from the statistical retrieval needs to be below 20 $\mathrm{g\ m^{-2}}$, which is in the order of the retrieval uncertainty. To avoid scenes with large scale advection of moist or dry air, the difference between the maximum and minimum $\mathrm{IWV_z}$ within one hour around the scan needs to be smaller than 2 $\mathrm{kg\ m^{-2}}$, which is above the instrument sensitivity. These requirements need to be fulfilled for at least three consecutive scans. The first and last scan of each sequence is neglected. The choice of the thresholds showed to be a good trade-off between excluding apparent cloudy situations, but still allowing a sufficient number of scans to generate a large data sample. Only the months between April and September between 2012–2018 are regarded, since the highest diurnal IWV variability is observed between spring and autumn at JOYCE (Löhnert et al., 2015) and the influence from the land surface is expected to be larger. During the observational period 316 days with in total 7261 single scans are selected with a mean $\mathrm{IWV_z}$ of 18.00 ± 6.37 $\mathrm{kg\ m^{-2}}$ measured in a 1 h window around the scans.

Instead of using the total slant column IWV, the humidity profile is integrated up to a scaling height of 2.5 km (hereafter: $\mathrm{IWV_{2.5}}$) for an analysis of the lower tropospheric water vapor patterns. This height, where the humidity profile drops below $1/e$, was found as mean value for the zenith MWR measurements 1 h around each of the selected scans. A similar scaling height was also found using satellite data (Simon and Joshi, 1994). For all scans, the mean value per scan is subtracted to investigate the deviations in each azimuth direction. In addition, a co-located Doppler lidar is used to gain information on atmospheric turbulence, wind direction and wind speed during the scans. The temporal resolution of the Doppler lidar VAD scans is 15 min and the closest measurement to the scan time is selected. For the general development of the wind direction during the day, 6 h

Atmos. Chem. Phys. Discuss., https://doi.org/10.5194/acp-2019-322
Manuscript under review for journal Atmos. Chem. Phys.
Discussion started: 7 May 2019

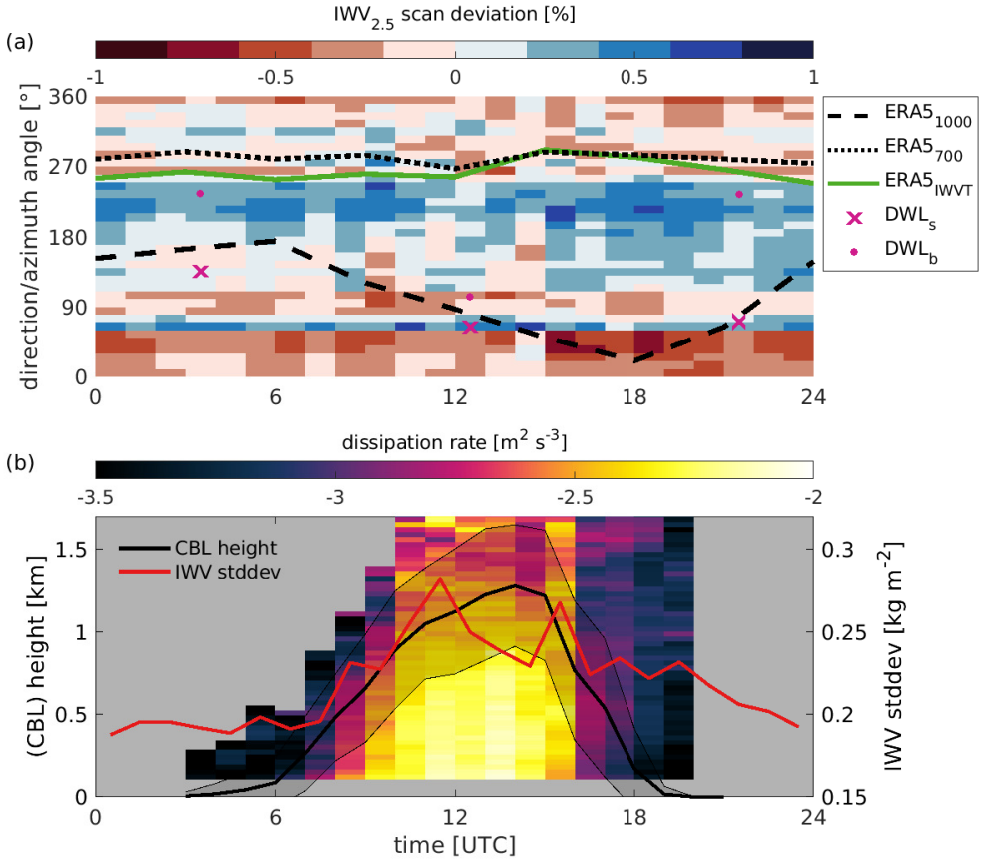

Figure 2. (a) Hourly mean values of the water vapor deviation (integrated up to 2.5 km) from the mean per MWR scan ($IWV_{2.5}$, number of scans: 7261), binned for all 36 azimuth directions. The lines show the directions (in degree) of the averaged ERA5 wind directions at 1000 hPa ($ERA5_{1000}$), 700 hPa ($ERA5_{700}$) and the IWV transport ($ERA5_{IWVT}$). Symbols indicate the mean Doppler lidar wind direction (average times: 01–06 UTC, 10–15 UTC, 19–24 UTC) at 105 m (DWL_s) and 1005 m (DWL_b). (b) Hourly averaged TKE dissipation rate and convective boundary-layer (CBL) height (with standard deviation in shadings) from the Doppler lidar boundary-layer classification at the MWR scan times. The zenith IWV standard deviation (stddev) is determined within 1 h around the scans.

averages are calculated.

Figure 2(a) shows the hourly mean value of the $IWV_{2.5}$ deviation binned for all 36 azimuth directions. A positive deviation up to 0.87% from the mean between 180–250° is visible throughout the day, with a shift to south-southeast during the afternoon and evening hours. Also a positive peak around 75° is present, showing no variations during the day. The number of scans per hour that are included in calculating the deviation ranges from 127 to 496 with less scans during midday. The decrease

Atmos. Chem. Phys. Discuss., https://doi.org/10.5194/acp-2019-322
Manuscript under review for journal Atmos. Chem. Phys.
Discussion started: 7 May 2019

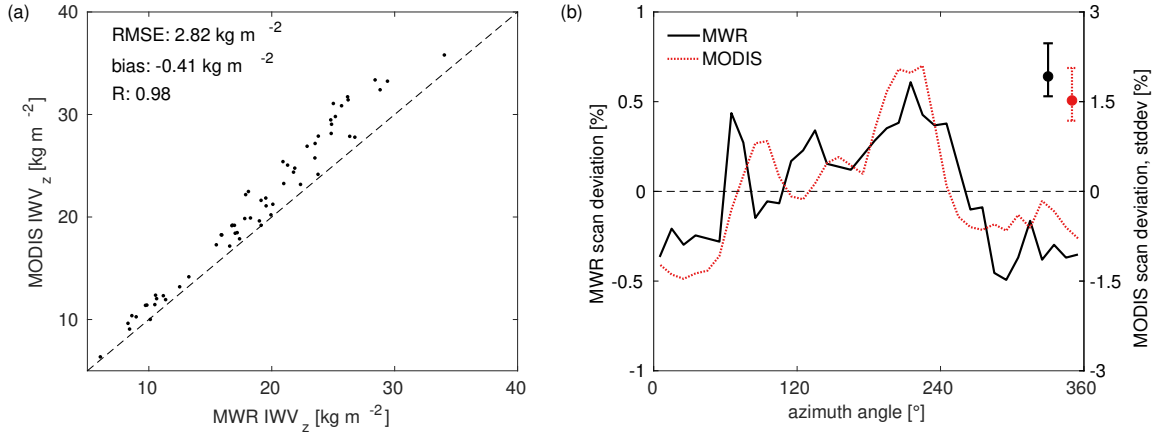

Figure 3. (a) Scatter-plot of the mean zenith IWV derived from the MWR ($\mathrm{IWV_{z,MWR}}$) within 1 h around the scans and MODIS measurements ($\mathrm{IWV_{z,MODIS}}$) within a 1 km radius. (b) Mean values of the $\mathrm{IWV_{2.5}}$ deviations from the MWR scans around 1 h around the MODIS overpass and the corresponding MODIS IWV deviations for the cases in (a) including 61 MODIS overpasses and 172 MWR scans. The range and the median of the standard deviation for all scans is indicated by the vertical lines and dots, respectively.

in number of cases during daytime is due to the formation of convective clouds, since overcast situations would influence the number of cases independent of the time of the day. Also the mean standard deviation for each scan increases from 1.1% to 1.94% during daytime indicating the influence of convective activity, which is shown by high TKE dissipation rates and a mean CBL height up to 1.28 km (Fig. 2(b)). Note that these deviations are median values to detect the long-term pattern and that single scan deviations from the mean can get over 5%. Also the IWV standard deviation from the zenith MWR measurements in Fig. 2(b) reveals a diurnal cycle during this measurement period of late spring until early autumn, which is in agreement with the seasonal statistics derived in Löhnert et al. (2015). While the IWV standard deviation follows the rate of the CBL height development in the morning hours, an abrupt decrease is only evident in the turbulence measurements in the afternoon transition period. This suggests that water vapor is mixed into the upper layers of the atmosphere during daytime and is still present in the residual layer throughout the night and would explain the consistent pattern after sunset in Fig. 2(a).

Separating all cases according to the low-level wind direction from the Doppler lidar, no directional dependence is found. For assessing the impact of the large scale water vapor transport, the ERA5 reanalysis product is used. The ERA5 IWV at the closest output time to the MWR scans compared to the 1 h averaged $\mathrm{IWV_z}$ from the MWR shows a high correlation coefficient of 0.98 and a root-mean-square error (RMSE) of only 1.46 $\mathrm{kg\ m^{-2}}$. The ERA5 wind direction at 1000 hPa ($\mathrm{ERA5_{1000}}$) is in good agreement with the mean near surface wind direction (average times: 01–06 UTC, 10–15 UTC, 19–24 UTC) derived from the Doppler lidar at 105 m ($\mathrm{DWL_s}$, Fig. 2(a)). The wind direction ranges from a southerly flow during night to an east to north direction during the day corresponding to fair weather situations and anticyclonic flow at this site. The wind direction turns clockwise with height for the ERA5 product and the Doppler lidar observations, but stays relatively constant within the CBL

as there is no large difference between $\mathrm{DWL_s}$ and the Doppler lidar wind direction at 1005 m ($\mathrm{DWL_b}$) between 10–15 UTC. The wind direction in the free troposphere at 700 hPa shows no significant diurnal cycle. The same applies to the IWVT, that corresponds to the westerly wind direction at 700 hPa, showing the west-wind-zone transport of humid air at the mid-latitudes, which might contribute to the $\mathrm{IWV_{2.5}}$ deviation scan pattern, especially during night. But at midday and early afternoon the positive deviations increase and shift to the southeast. Despite the fact, that the ERA5 IWV shows a diurnal cycle, this shift can not be seen in the IWVT, suggesting that also local influences contribute to the observed IWV signal. This is further analyzed in the next section.

3.2 Comparison of daytime MWR and MODIS derived IWV deviations

For a comparison with an independent IWV measurement, the MWR results are compared to the MODIS-NIR derived IWV around JOYCE. For a fair comparison of the column amount of water vapor from MODIS to the path-integrated water vapor observations from the MWR scans, a virtual MWR scan is derived from the MODIS observations. Therefore, the total IWV is distributed to an absolute humidity profile assuming a linear decrease by 20% in the CBL and an exponential decrease above similar to Schween et al. (2011). The CBL height is determined from the boundary-layer classification (Manninen et al., 2018) available for each overpass. The CBL height is assumed to be constant in the area of interest, as well as the $1/e$ height for the exponential decrease, which is calculated from the MWR humidity profile. In this way a virtual scan corresponding to the MWR scan configuration can be performed around JOYCE where the amount of water vapor is integrated for each beam. Only overpasses without missing data due to the MODIS quality checks are considered. A circular area with a radius of 4.3 km is chosen. This radius corresponds to the distance, where the beam at 30° reaches the water vapor scaling height of 2.5 km, which was found on average in the zenith MWR humidity measurements.

As an additional comparison of MWR and MODIS, the $\mathrm{IWV_z}$ measurements of the MWR ($\mathrm{IWV_{z,MWR}}$) and the MODIS mean total column amount 1 km around JOYCE ($\mathrm{IWV_{z,MODIS}}$) are compared (Fig. 3(a)). The zenith IWV values are highly correlated (0.98) with a RMSE of 2.79 $\mathrm{kg\,m^{-2}}$, which is about 1 $\mathrm{kg\,m^{-2}}$ higher than found in Steinke et al. (2015). This discrepancy is probably caused by a greater IWV variability shown in Fig. 2(b). For larger IWV values, the MODIS observations tend to an overestimation. For the 61 MODIS overpasses occurring between 9–13 UTC, the corresponding MWR scans within 1 h around the overpass are selected (172 scans) and for both data sets the mean IWV deviation from the (virtual) scans are calculated (Fig. 3(b)). In general, the relative deviations from the MODIS virtual scans are higher by a factor of about 3. With both observations, a noticeable negative deviation between 270°–60° is visible, but also the agreement in the location of the maximum positive deviations around 225° is evident. This area shows a high fraction of crop and grassland and one of the pit mines, whereas less water vapor seems to be present in the vicinity of the urban area and forested hill. Regarding the MODIS derived results, also the pit mine around 90° reveals a positive deviation, but the peak for the MWR is shifted. This phenomena might be explained by the orographic flow which is strongly altered by the pit mines as shown in Marke et al. (2018) and the low spatial resolution of the MODIS IWV product. The results suggest a higher water vapor flux into the atmosphere for the agricultural fields due to evapotranspiration and the high amount of water vapor around the pit mines

Atmos. Chem. Phys. Discuss., https://doi.org/10.5194/acp-2019-322
Manuscript under review for journal Atmos. Chem. Phys.
Discussion started: 7 May 2019

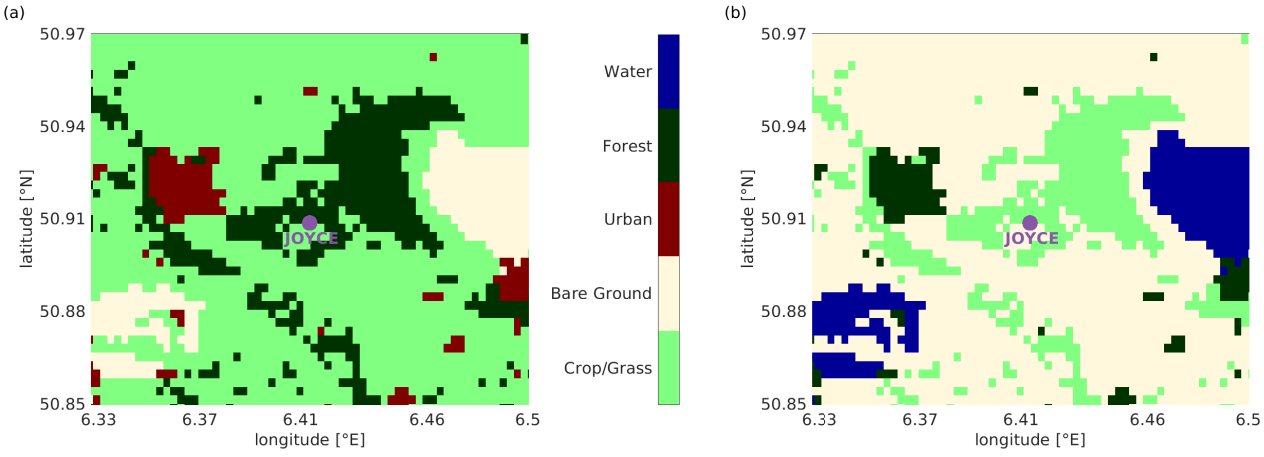

Figure 4. (a) 12x13 km map of the simplified GLOBCOVER land use data centered around JOYCE used for the first ICON-LEM simulation (ICON1). (b) Same as (a) but with altered land use types for the second simulation (ICON2).

could be caused by irrigation to reduce dust emissions during the day and dew formation at night. In contrast, the forest and urban areas reveal a lower water vapor amount. This can be explained by less water availability in urban areas and a higher water use efficiency for deciduous forests compared to crop fields demonstrated in Tang et al. (2015). A similar difference in the surface fluxes between crops during the main vegetation period and forest (pine trees) was found using surface flux measurements (Beyrich et al., 2006) and in the LES study by Garcia-Carreras et al. (2011). In addition, lower wind speeds due to the topography and a higher roughness length at the forested hill can cause decreased water vapor fluxes into the atmosphere.

3.3 LES case study analysis

The influence of the land use type on the atmospheric water vapor pattern is further investigated in a case study (25 July 2012) by means of a large-eddy simulation using the ICON-LEM model. On this day, with a northwesterly wind direction, no clouds are observed until 12:30 UTC and the timings of the MODIS overpasses are 10:00 UTC and 11:40 UTC. In this time interval, four MWR scans are performed and the CBL height determined by the Doppler lidar increases from 885 m to 1305 m. In the first ICON-LEM simulation (ICON1) using the simplified GLOBCOVER land use data (Fig. 4(a)), the model boundary-layer height reaches these heights about one hour later than in the observations. In order to compare a similar state of the boundary-layer in terms of convection, the analysis time for the simulations is shifted by one hour. Again, like for the MODIS data, a virtual scan at 30° elevation is constructed and the absolute humidity is integrated up to 2.5 km. The mean $\mathrm{IWV_z}$ values are 24.83 $\mathrm{kg\ m^{-2}}$ (MWR), 29.26 $\mathrm{kg\ m^{-2}}$ (MODIS) and 28.22 $\mathrm{kg\ m^{-2}}$ (ICON1), where the ICON1 zenith IWV is averaged within a radius of 1 km around JOYCE and for MODIS the nearest pixel is chosen.

Atmos. Chem. Phys. Discuss., https://doi.org/10.5194/acp-2019-322
Manuscript under review for journal Atmos. Chem. Phys.
Discussion started: 7 May 2019

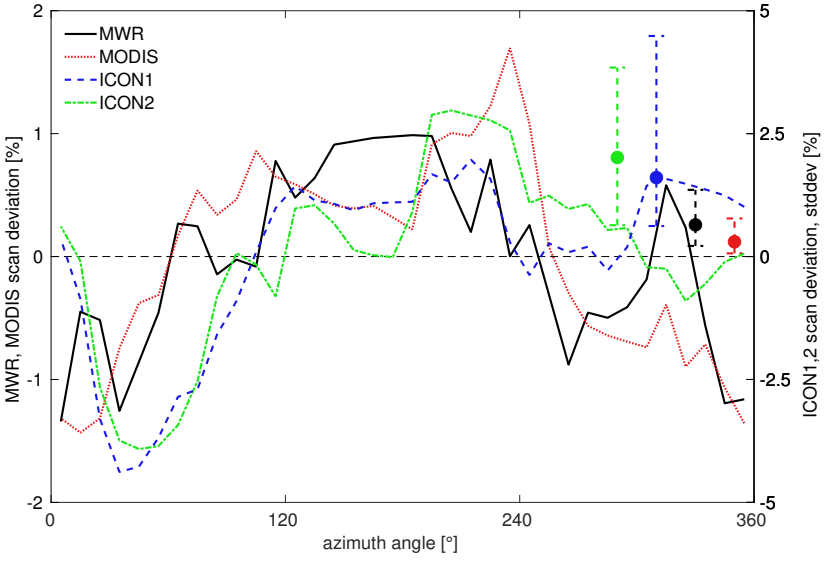

Figure 5. Same as Fig. 3(b), but for the 25 July 2012 case study including four MWR scans (10:15–11:10 UTC), two MODIS overpasses (10:00 UTC, 11:40 UTC) and the ICON1, ICON2 simulations between 11:20–12:10 UTC.

Figure 5 shows the results of the comparison between the MWR, MODIS and ICON scans. As already shown in the previous long-term analysis, the maximum positive deviation occurs in a southerly direction with a good agreement in the sign changes between MWR and MODIS. For ICON1, the northeastern minimum deviation can be seen, but a higher positive deviation in the northwest is visible compared to MODIS and MWR. This might be due to a smaller extent of the urban area (4.8%) in the land use data with 300 m resolution, where small scale features are not resolved, compared to 18.5% in the land use classification shown in Fig. 1. Also a more dominant large scale humidity transport in the simulations could be a reason. The positive peak around the direction of the eastern pit mine is missed in ICON1, probably because of a different position, extent and depth of the mine for the production period of the GLOBCOVER data (2009) compared to the year of the simulation (2012).

In a second simulation (ICON2), the land use types are changed according to Fig. 4(b) (crop/grass to bare ground, bare ground to water, urban to forest, forest to crop/grass and water to urban). In this way, a significant reconstruction in the spatial distribution of the land use types is achieved without changing the scale of heterogeneity. The comparison in the IWV deviation between ICON1 and ICON2 shows higher IWV values in the northwest for ICON1 and in the southwest for ICON2. To elaborate the details of this difference, the spatial fields of height and time averaged vertical velocity and mean IWV are analyzed (Fig. 6). The averaging domain is the same as shown in Fig. 4 and the averaging time is between 12–13 UTC, which is the time range of the first cloud formation in the simulations. Poll et al. (2017) also performed large-eddy simulations of this day in a similar domain and showed the occurrence of clouds around this time in visible satellite data. They found cellular structures

Atmos. Chem. Phys. Discuss., https://doi.org/10.5194/acp-2019-322
Manuscript under review for journal Atmos. Chem. Phys.
Discussion started: 7 May 2019

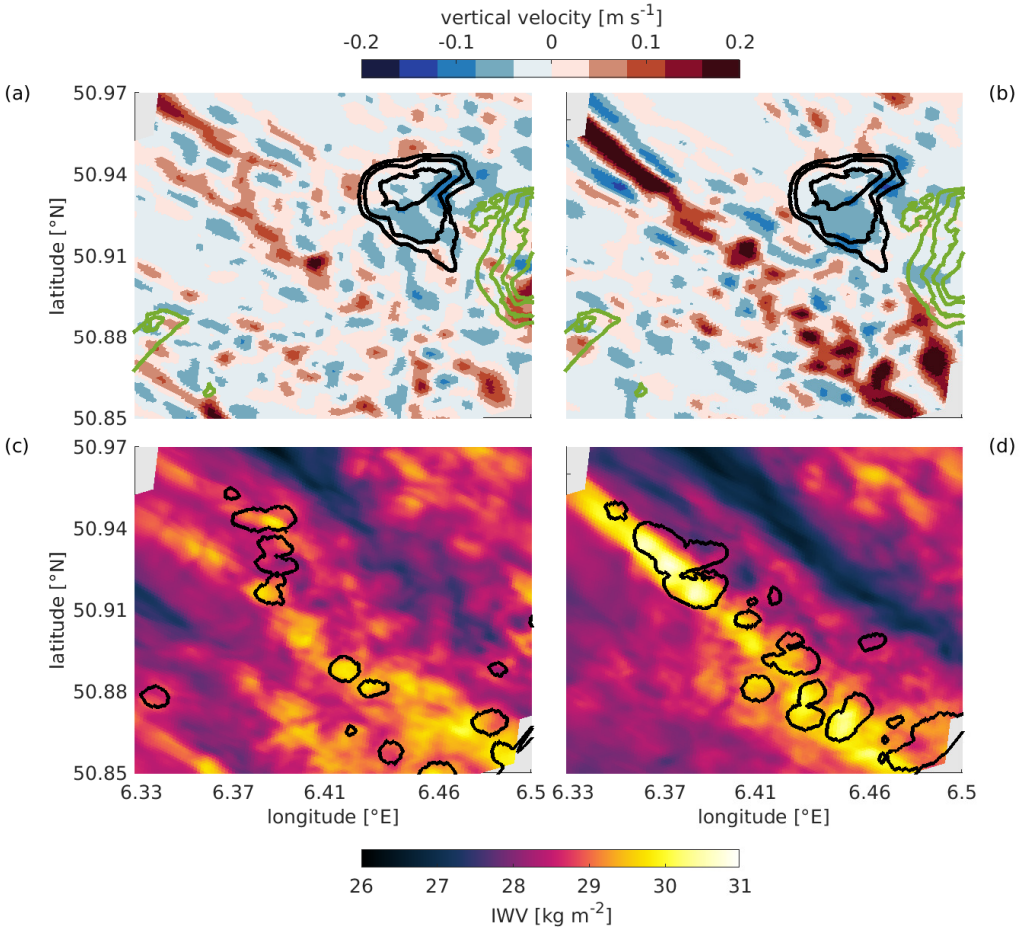

Figure 6. ICON-LEM vertically averaged vertical velocity (top) and IWV (bottom) of the ICON1 (a,c) and ICON2 (b,d) simulations. Contours in (a), (b) refer to the topography relative to JOYCE in m a.s.l. between -200 m to 0 m (green) and 0 m to 200 m (black) in 50 m steps. Contours in (c), (d) show areas with total column integrated cloud water values above 10 $\mathrm{g\ m^{-2}}$. The results are averaged between 12–13 UTC.

regarding the vertical velocity, which is also evident in Fig. 6(a). In addition, the wind is lifted by the hill and a downdraft above the hill can be seen. This was already discussed in Marke et al. (2018) and might explain parts of the lower water vapor flux discussed in Sect. 3.1. In the ICON2 simulation, with a larger fraction of bare ground, the differences in surface properties and the size of the heterogeneous land use patches seem to be large enough to cause a secondary circulation (Garcia-Carreras et al., 2011; van Heerwaarden et al., 2014; Eder et al., 2015) resulting in roll structures of the vertical velocity. Less vegetated areas also lead to an increase in the mean wind speed of 0.42 $\mathrm{m\ s^{-1}}$ at approximately 200 m above ground.

Atmos. Chem. Phys. Discuss., https://doi.org/10.5194/acp-2019-322
Manuscript under review for journal Atmos. Chem. Phys.
Discussion started: 7 May 2019

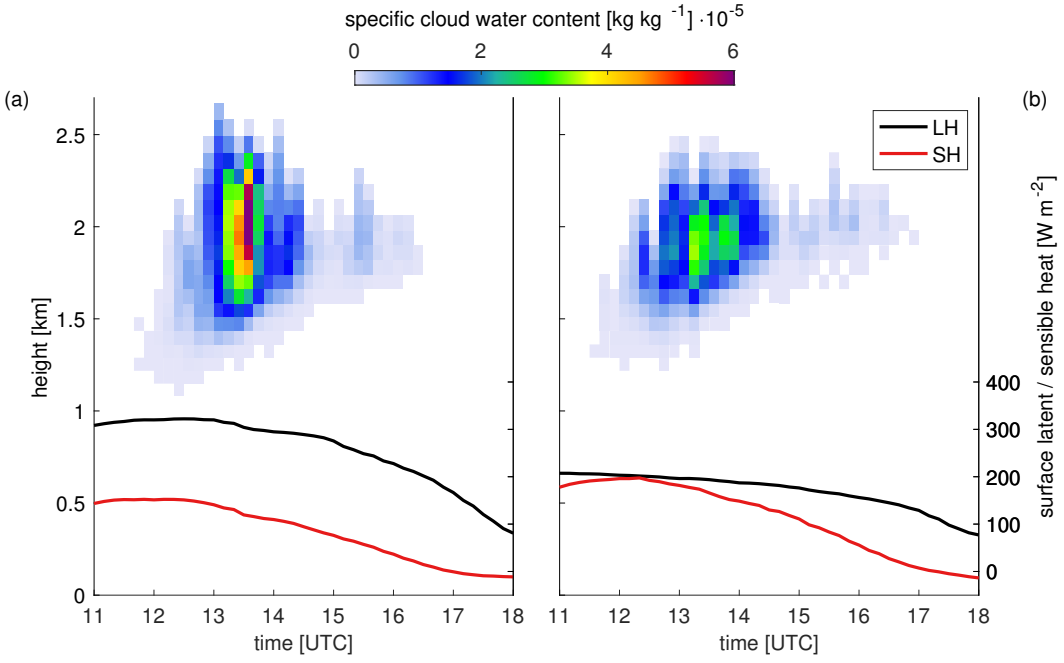

Figure 7. ICON-LEM specific cloud water content for the ICON1 (a) and ICON2 (b) simulation together with the surface fluxes of latent and sensible heat. The results are averaged for the domain shown in Fig. 4.

The change in the circulation pattern due to the different land use input can explain the differences in IWV deviation (Fig. 5), since more water vapor is transported in the enhanced updraft streak (Fig. 6(d)). The strong circulation effect might also reduce the influence of other humidity sources, like the introduced water bodies at the positions of the pit mines in ICON2. The formation of convective clouds in the simulations is affected as well. Whereas in ICON1 the cloud distribution is rather patchy, clouds form only along the high IWV region in ICON2. Also the mean cloud cover of 8.55% in ICON1 compared to 10.55% in ICON2 is closer to the observed maximum cloud cover of 6% determined by a total sky imager at JOYCE. The maximum integrated cloud water content of these clouds is 36.96 $\mathrm{g\ m^{-2}}$ (ICON1) and 5.61 $\mathrm{g\ m^{-2}}$ (ICON2). The specific cloud water content in ICON1 is significantly higher and the clouds grow taller compared to the ICON2 simulation (Fig. 7), which is connected to a higher latent heat flux in ICON1 due to more vegetated areas. On the other side the boundary-layer grows deeper (by about 30 m) in ICON2 because of the increased sensible heat flux caused by a higher fraction of bare ground. This shows the connections of the different Earth system compartments and stresses the importance of further monitoring and modeling the interactions between the land use, water vapor and the transition to clouds.

Atmos. Chem. Phys. Discuss., https://doi.org/10.5194/acp-2019-322
Manuscript under review for journal Atmos. Chem. Phys.
Discussion started: 7 May 2019

4 Conclusions

Exchange processes between the land surface and atmosphere are an important controlling factor in the water cycle. Long-term observational evidence of this interaction in scales of a few kilometers is still lacking. The scanning microwave radiometer (MWR) at the Jülich ObservatorY for Cloud Evolution (JOYCE) proved to suitable for detecting spatial IWV deviations for single scans, but also in a statistical sense. The atmospheric water vapor pattern can only partly be explained by the large-scale driven advection and is attributed to the local transport of water vapor from the surface, especially during convective scenes. This is detected in the the long-term analysis of over 7200 liquid water cloud free scans within six years of observations.

The comparison to the satellite-based MODIS near-infrared IWV product, as an independent observation, shows similar features of areas with pronounced positive and negative deviations around JOYCE. In a further step, these deviations can be related qualitatively to land surface properties by means of a land use classification. The classification is based on a remote sensing derived regional crop map and reveals, that positive IWV deviations mainly originate over agriculture areas and open pit mines close to the measurement site, while urban and elevated forest areas show negative deviations. The locations of the maximum and minimum deviation in the MODIS and MWR measurements are in agreement.

In a comprehensive case study, large-eddy simulations by the high resolution ICON-LEM model are carried out to further assess the impact of the land surface on the atmospheric water vapor field. While the control simulation with a realistic land use input showed similar characteristics of spatial IWV deviations, the second simulation with modified land use types revealed changes in the mesoscale circulation, cloud characteristics and IWV distribution according to the altered land surface. These findings suggest that ground-based remote sensing of water vapor supported by high resolution modeling can be valuable for studying the regional influence of heterogeneous land surfaces on the atmospheric water vapor and the connection between surface fluxes, water vapor and clouds.

Author contributions. TM, SC and UL designed the experiments and processed the observational data. VS performed the ICON-LEM simulations and TM prepared the manuscript with contributions from all co-authors.

Competing interests. The authors declare that they have no conflict of interest.

Acknowledgements. The authors would like to acknowledge the Transregional Collaborative Research Centre (TR32) "Patterns in Soil-Vegetation-Atmosphere Systems" funded by the German Science Foundation (DFG), which has continuously contributed to the instrumentation of JOYCE-CF and its maintenance as well as funding T. Marke. Further, the Humidity And Temperature PROfiler (HATPRO) used in this study have been funded by DFG infrastructural programs under the grant INST 216/681-1. The MODIS/Terra Total Precipitable Water

Atmos. Chem. Phys. Discuss., https://doi.org/10.5194/acp-2019-322
Manuscript under review for journal Atmos. Chem. Phys.
Discussion started: 7 May 2019

Atmospheric Chemistry and Physics Discussions

Vapor 5-Min L2 Swath 1km dataset was acquired from the Level-1 and Atmosphere Archive & Distribution System (LAADS) Distributed Active Archive Center (DAAC), located in the Goddard Space Flight Center in Greenbelt, Maryland (https://ladsweb.nascom.nasa.gov/).

References

Adler, B., Kalthoff, N., Kohler, M., Handwerker, J., Wieser, A., Corsmeier, U., Kottmeier, C., Lambert, D., and Bock, O.: The variability of water vapour and pre-convective conditions over the mountainous island of Corsica, Quarterly Journal of the Royal Meteorological Society, 142, 335–346, https://doi.org/10.1002/qj.2545, 2016.

Avissar, R. and Schmidt, T.: An Evaluation of the Scale at which Ground-Surface Heat Flux Patchiness Affects the Convective Boundary Layer Using Large-Eddy Simulations, Journal of the Atmospheric Sciences, 55, 2666–2689, https://doi.org/10.1175/1520-0469(1998)055<2666:aeotsa>2.0.co;2, 1998.

Beyrich, F., Leps, J.-P., Mauder, M., Bange, J., Foken, T., Huneke, S., Lohse, H., Lüdi, A., Meijninger, W. M. L., Mironov, D., Weisensee, U., and Zittel, P.: Area-Averaged Surface Fluxes Over the Litfass Region Based on Eddy-Covariance Measurements, Boundary-Layer Meteorology, 121, 33–65, https://doi.org/10.1007/s10546-006-9052-x, 2006.

Bontemps, S., Defourny, P., Van Bogaert, E., Arino, O., Kalogirou, V., and Ramos Perez, J. J.: GLOBCOVER 2009 Products Description and Validation Report, Université catholique de Louvain (UCL) & European Space Agency (ESA), 2.2, 53 pp, 2011.

Clark, C. A. and Arritt, P. W.: Numerical Simulations of the Effect of Soil Moisture and Vegetation Cover on the Development of Deep Convection, Journal of Applied Meteorology, 34, 2029–2045, https://doi.org/10.1175/1520-0450(1995)034<2029:NSOTEO>2.0.CO;2, 1995.

Copernicus Climate Change Service (C3S): ERA5: Fifth generation of ECMWF atmospheric reanalyses of the global climate. Copernicus Climate Change Service Climate Data Store (CDS), Copernicus Climate Change Service Climate Data Store (CDS), date of access: 03/03/2019, 2017.

Courault, D., Drobinski, P., Brunet, Y., Lacarrere, P., and Talbot, C.: Impact of surface heterogeneity on a buoyancy-driven convective boundary layer in light winds, Boundary-Layer Meteorology, 124, 383–403, https://doi.org/10.1007/s10546-007-9172-y, 2007.

Eder, F., De Roo, F., Rotenberg, E., Yakir, D., Schmid, H. P., and Mauder, M.: Secondary circulations at a solitary forest surrounded by semi-arid shrubland and their impact on eddy-covariance measurements, Agricultural and Forest Meteorology, 211-212, 115–127, https://doi.org/10.1016/j.agrformet.2015.06.001, 2015.

Gao, B.-C. and Kaufman, Y. J.: Water vapor retrievals using Moderate Resolution Imaging Spectroradiometer (MODIS) near-infrared channels, Journal of Geophysical Research: Atmospheres, 108, https://doi.org/10.1029/2002jd003023, 2003.

Garcia-Carreras, L., Parker, D. J., and Marsham, J. H.: What is the Mechanism for the Modification of Convective Cloud Distributions by Land Surface–Induced Flows?, Journal of the Atmospheric Sciences, 68, 619–634, https://doi.org/10.1175/2010jas3604.1, 2011.

Heinze, R., Dipankar, A., Henken, C. C., Moseley, C., Sourdeval, O., Trömel, S., Xie, X., Adamidis, P., Ament, F., Baars, H., Barthlott, C., Behrendt, A., Blahak, U., Bley, S., Brdar, S., Brueck, M., Crewell, S., Deneke, H., Di Girolamo, P., Evaristo, R., Fischer, J., Frank, C., Friederichs, P., Göcke, T., Gorges, K., Hande, L., Hanke, M., Hansen, A., Hege, H.-C., Hoose, C., Jahns, T., Kalthoff, N., Klocke, D., Kneifel, S., Knippertz, P., Kuhn, A., van Laar, T., Macke, A., Maurer, V., Mayer, B., Meyer, C. I., Muppa, S. K., Neggers, R. A. J., Orlandi, E., Pantillon, F., Pospichal, B., Röber, N., Scheck, L., Seifert, A., Seifert, P., Senf, F., Siligam, P., Simmer, C., Steinke, S., Stevens, B., Wapler, K., Weniger, M., Wulfmeyer, V., Zängl, G., Zhang, D., and Quaas, J.: Large-eddy simulations over Germany using ICON: a comprehensive evaluation: Evaluation of ICON in Realistic LES Configuration, Quarterly Journal of the Royal Meteorological Society, 143, 69–100, https://doi.org/10.1002/qj.2947, 2017.

Huang, H. Y. and Margulis, S. A.: On the impact of surface heterogeneity on a realistic convective boundary layer, Water Resources Research, 45, https://doi.org/10.1029/2008WR007175, 2009.

Kneifel, S., Crewell, S., Lohnert, U., and Schween, J.: Investigating Water Vapor Variability by Ground-Based Microwave Radiometry: Evaluation Using Airborne Observations, IEEE Geoscience and Remote Sensing Letters, 6, 157–161, https://doi.org/10.1109/LGRS.2008.2007659, 2009.

Löhnert, U. and Crewell, S.: Accuracy of cloud liquid water path from ground-based microwave radiometry 1. Dependency on cloud model statistics, Radio Science, 38, https://doi.org/10.1029/2002rs002654, 2003.

Löhnert, U., Schween, J. H., Acquistapace, C., Ebell, K., Maahn, M., Barrera-Verdejo, M., Hirsikko, A., Bohn, B., Knaps, A., O'Connor, E., Simmer, C., Wahner, A., and Crewell, S.: JOYCE: Jülich Observatory for Cloud Evolution, Bulletin of the American Meteorological Society, 96, 1157–1174, https://doi.org/10.1175/BAMS-D-14-00105.1, https://doi.org/10.1175/BAMS-D-14-00105.1, 2015.

Macke, A., Seifert, P., Baars, H., Barthlott, C., Beekmans, C., Behrendt, A., Bohn, B., Brueck, M., Bühl, J., Crewell, S., Damian, T., Deneke, H., Düsing, S., Foth, A., Di Girolamo, P., Hammann, E., Heinze, R., Hirsikko, A., Kalisch, J., Kalthoff, N., Kinne, S., Kohler, M., Löhnert, U., Madhavan, B. L., Maurer, V., Muppa, S. K., Schween, J., Serikov, I., Siebert, H., Simmer, C., Späth, F., Steinke, S., Träumner, K., Trömel, S., Wehner, B., Wieser, A., Wulfmeyer, V., and Xie, X.: The {HD}({CP})² {Observational} {Prototype} {Experiment} ({HOPE}) – an overview, Atmospheric Chemistry and Physics, 17, 4887–4914, https://doi.org/10.5194/acp-17-4887-2017, 2017.

Manninen, A. J., Marke, T., Tuononen, M., and O'Connor, E. J.: Atmospheric Boundary Layer Classification With Doppler Lidar, Journal of Geophysical Research: Atmospheres, 123, 8172–8189, https://doi.org/10.1029/2017JD028169, 2018.

Marke, T., Crewell, S., Schemann, V., Schween, J. H., and Tuononen, M.: Long-term observations and high-resolution modeling of midlatitude nocturnal boundary layer processes connected to low-level jets, Journal of Applied Meteorology and Climatology, 57, 1155–1170, https://doi.org/10.1175/JAMC-D-17-0341.1, 2018.

Maronga, B. and Raasch, S.: Large-Eddy Simulations of Surface Heterogeneity Effects on the Convective Boundary Layer During the LITFASS-2003 Experiment, Boundary-Layer Meteorology, 146, 17–44, https://doi.org/10.1007/s10546-012-9748-z, 2013.

Maschwitz, G., Löhnert, U., Crewell, S., Rose, T., and Turner, D. D.: Investigation of ground-based microwave radiometer calibration techniques at 530 hPa, Atmospheric Measurement Techniques, 6, 2641–2658, https://doi.org/10.5194/amt-6-2641-2013, 2013.

O'Connor, E. J., Illingworth, A. J., Brooks, I. M., Westbrook, C. D., Hogan, R. J., Davies, F., Brooks, and J., B.: A method for estimating the turbulent kinetic energy dissipation rate from a vertically pointing doppler lidar, and independent evaluation from balloon-borne in situ measurements, Journal of Atmospheric and Oceanic Technology, 27, 1652–1664, https://doi.org/10.1175/2010JTECHA1455.1, 2010.

Ookouchi, Y., Segal, M., Kessler, R. C., and Pielke, R. A.: Evaluation of Soil Moisture Effects on the Generation and Modification of Mesoscale Circulations, Monthly Weather Review, 112, 2281–2292, https://doi.org/10.1175/1520-0493(1984)112<2281:eosmeo>2.0.co;2, 1984.

Pearson, G., Davies, F., and Collier, C.: An Analysis of the Performance of the UFAM Pulsed Doppler Lidar for Observing the Boundary Layer, Journal of Atmospheric and Oceanic Technology, 26, 240–250, https://doi.org/10.1175/2008JTECHA1128.1, 2009.

Pielke, R. A., Dalu, G. A., Snook, J. S., Lee, T. J., and Kittel, T. G. F.: Nonlinear Influence of Mesoscale Land Use on Weather and Climate, Journal of Climate, 4, 1053–1069, https://doi.org/10.1175/1520-0442(1991)004<1053:niomlu>2.0.co;2, 1991.

Poll, S., Shrestha, P., and Simmer, C.: Modelling convectively induced secondary circulations in the *terra incognita* with TerrSysMP: Modelling CISCs in the Terra Incognita with TerrSysMP, Quarterly Journal of the Royal Meteorological Society, 143, 2352–2361, https://doi.org/10.1002/qj.3088, 2017.

Rabin, R. M., Stadler, S., Wetzel, P. J., Stensrud, D. J., and Gregory, M.: Observed Effects of Landscape Variability on Convective Clouds, Bulletin of the American Meteorological Society, 71, 272–280, https://doi.org/10.1175/1520-0477(1990)071<0272:oeolvo>2.0.co;2, 1990.

Rose, T., Crewell, S., Löhnert, U., and Simmer, C.: A network suitable microwave radiometer for operational monitoring of the cloudy atmosphere, Atmospheric Research, 75, 183–200, https://doi.org/10.1016/j.atmosres.2004.12.005, 2005.

Schween, J. H., Crewell, S., and Löhnert, U.: Horizontal-humidity gradient from one single-scanning microwave radiometer, IEEE Geoscience and Remote Sensing Letters, 8, 336–340, https://doi.org/10.1109/LGRS.2010.2072981, 2011.

Shao, Y., Liu, S., Schween, J. H., and Crewell, S.: Large-Eddy Atmosphere–Land-Surface Modelling over Heterogeneous Surfaces: Model Development and Comparison with Measurements, Boundary-Layer Meteorology, 148, 333–356, https://doi.org/10.1007/s10546-013-9823-0, 2013.

Simmer, C., Thiele-Eich, I., Masbou, M., Amelung, W., Bogena, H., Crewell, S., Diekkrüger, B., Ewert, F., Hendricks Franssen, H.-J., Huisman, J. A., Kemna, A., Klitzsch, N., Kollet, S., Langensiepen, M., Löhnert, U., Rahman, A. S. M. M., Rascher, U., Schneider, K., Schween, J., Shao, Y., Shrestha, P., Stiebler, M., Sulis, M., Vanderborght, J., Vereecken, H., van der Kruk, J., Waldhoff, G., and Zerenner, T.: Monitoring and Modeling the Terrestrial System from Pores to Catchments: The Transregional Collaborative Research Center on Patterns in the Soil–Vegetation–Atmosphere System, Bulletin of the American Meteorological Society, 96, 1765–1787, https://doi.org/10.1175/BAMS-D-13-00134.1, 2015.

Simon, B. and Joshi, P. C.: Determination of moisture changes prior to the onset of south-west monsoon over Kerala using NOAA/TOVS satellite data, Meteorology and Atmospheric Physics, 53, 223–231, https://doi.org/10.1007/BF01029613, 1994.

Späth, F., Behrendt, A., Kumar Muppa, S., Metzendorf, S., Riede, A., and Wulfmeyer, V.: 3-D water vapor field in the atmospheric boundary layer observed with scanning differential absorption lidar, Atmospheric Measurement Techniques, 9, 1701–1720, https://doi.org/10.5194/amt-9-1701-2016, 2016.

Steinke, S., Eikenberg, S., Löhnert, U., Dick, G., Klocke, D., Di Girolamo, P., and Crewell, S.: Assessment of small-scale integrated water vapour variability during HOPE, Atmospheric Chemistry and Physics, 15, 2675–2692, https://doi.org/10.5194/acp-15-2675-2015, 2015.

Tang, X., Li, H., Desai, A. R., Nagy, Z., Luo, J., Kolb, T. E., Olioso, A., Xu, X., Yao, L., Kutsch, W., Pilegaard, K., Köstner, B., and Ammann, C.: How is water-use efficiency of terrestrial ecosystems distributed and changing on Earth?, Scientific Reports, 4, https://doi.org/10.1038/srep07483, 2015.

van Heerwaarden, C. C. and Guerau de Arellano, J. V.: Relative Humidity as an Indicator for Cloud Formation over Heterogeneous Land Surfaces, Journal of the Atmospheric Sciences, 65, 3263–3277, https://doi.org/10.1175/2008JAS2591.1, 2008.

van Heerwaarden, C. C., Mellado, J. P., and De Lozar, A.: Scaling Laws for the Heterogeneously Heated Free Convective Boundary Layer, Journal of the Atmospheric Sciences, 71, 3975–4000, https://doi.org/10.1175/JAS-D-13-0383.1, 2014.

Vilà-Guerau De Arellano, J., Ouwersloot, H. G., Baldocchi, D., and Jacobs, C. M.: Shallow cumulus rooted in photosynthesis, Geophysical Research Letters, 41, 1796–1802, https://doi.org/10.1002/2014GL059279, 2014.

Waldhoff, G., Lussem, U., and Bareth, G.: Multi-Data Approach for remote sensing-based regional crop rotation mapping: A case study for the Rur catchment, Germany, International Journal of Applied Earth Observation and Geoinformation, 61, 55–69, https://doi.org/10.1016/j.jag.2017.04.009, 2017.

Weckwerth, T. M., Parsons, D. B., Koch, S. E., Moore, J. A., LeMone, M. A., Demoz, B. B., Flamant, C., Geerts, B., Wang, J., and Feltz, W. F.: An Overview of the International H_2O Project (IHOP_2002) and Some Preliminary Highlights, Bulletin of the American Meteorological Society, 85, 253–278, https://doi.org/10.1175/BAMS-85-2-253, 2004.

Wulfmeyer, V., Behrendt, A., Kottmeier, C., Corsmeier, U., Barthlott, C., Craig, G. C., Hagen, M., Althausen, D., Aoshima, F., Arpagaus, M., Bauer, H.-S., Bennett, L., Blyth, A., Brandau, C., Champollion, C., Crewell, S., Dick, G., Di Girolamo, P., Dorninger, M., Dufournet, Y., Eigenmann, R., Engelmann, R., Flamant, C., Foken, T., Gorgas, T., Grzeschik, M., Handwerker, J., Hauck, C., Höller, H., Junkermann, W.,

Kalthoff, N., Kiemle, C., Klink, S., König, M., Krauss, L., Long, C. N., Madonna, F., Mobbs, S., Neininger, B., Pal, S., Peters, G., Pigeon, G., Richard, E., Rotach, M. W., Russchenberg, H., Schwitalla, T., Smith, V., Steinacker, R., Trentmann, J., Turner, D. D., van Baelen, J., Vogt, S., Volkert, H., Weckwerth, T., Wernli, H., Wieser, A., and Wirth, M.: The Convective and Orographically-induced Precipitation Study (COPS): the scientific strategy, the field phase, and research highlights, Quarterly Journal of the Royal Meteorological Society, 137, 3–30, https://doi.org/10.1002/qj.752, 2011.

Wulfmeyer, V., Turner, D. D., Baker, B., Banta, R., Behrendt, A., Bonin, T., Brewer, W. A., Buban, M., Choukulkar, A., Dumas, E., Hardesty, R. M., Heus, T., Ingwersen, J., Lange, D., Lee, T. R., Metzendorf, S., Muppa, S. K., Meyers, T., Newsom, R., Osman, M., Raasch, S., Santanello, J., Senff, C., Späth, F., Wagner, T., and Weckwerth, T.: A New Research Approach for Observing and Characterizing Land-Atmosphere Feedback, Bulletin of the American Meteorological Society, 99, 1639–1667, https://doi.org/10.1175/BAMS-D-17-0009.1, 2018.

Zängl, G., Reinert, D., Rípodas, P., and Baldauf, M.: The ICON (ICOsahedral Non-hydrostatic) modelling framework of DWD and MPI-M: Description of the non-hydrostatic dynamical core, Quarterly Journal of the Royal Meteorological Society, 141, 563–579, https://doi.org/10.1002/qj.2378, 2015.